

Near-Field Optical Properties of Fully Alloyed Noble Metal Nanoparticles

Chen Gong, Mariama Rebello Sousa Dias, Garrett C. Wessler, Joshua A. Taillon, Lourdes G. Salamanca-Riba, and Marina S. Leite*

Combining metallic elements with different compositions at the nanoscale to obtain fully alloyed nanostructures can pave the way for an optical-electronic platform with fine-tunable response over a very broad range of the electromagnetic spectrum, from the UV to the IR. While the optical properties of pure metallic nanostructures have been extensively investigated by varying their size, shape and distribution, their intrinsic dielectric function still limits its application. Here, we implement the dewetting of metallic thin films to produce fully alloyed $\text{Ag}_x\text{Au}_{1-x}$ nanoparticles (NPs), and show how their chemical composition affects the optical response of the self-assembled arrays. As an example of how alloying can be used as an additional knob to tune the localized surface plasmon resonance (LSPR) of metallic nanostructure systems, we analyze the near-field optical properties of alloyed $\text{Ag}_{0.5}\text{Au}_{0.5}$ NPs by combining spectrally dependent near-field scanning optical microscopy (NSOM) with full-field simulations of the light-matter interactions. We find a strong variation in the absolute value of the electric field around and within the alloyed NPs. Our results demonstrate the potential of realizing alloyed nanostructures by a scalable method with engineered optical properties for applications ranging from nanophotonics to sensing.

LSPR is the confinement of the collective oscillation of the electron charges in metallic nanostructures, causing a pronounced electric field enhancement at their surface and high optical absorption. This property has been widely explored for Ag and Au NPs in the fields of nanophotonics,^[1,2] energy harvesting,^[3,4] molecular detection,^[5] biomedical therapeutics,^[6] and catalysis.^[7] The possibility of fabricating pure metallic NPs with controllable size and shape enables the modulation of the LSPR from the UV to the IR regions of the electromagnetic spectrum.^[8–11] However, the pressing need for providing on-demand plasmonic properties for nanophotonic applications still remains due to the fact that the optical response of pure metals, such as Ag and Au, is dominated by their intrinsic

dielectric function. Alloying of these noble metals has been applied to tune the material dielectric function, where the LSPR can be modulated progressively from the UV (pure Ag) to the NIR (pure Au).^[12–15] Thus, metallic nanostructures composed of Ag–Au can enable the rational design of building blocks for different applications, such as metamaterials,^[16,17] hot carrier devices,^[18] light absorption improvement in photovoltaics,^[19,20] colored glasses,^[21] displays,^[22,23] and catalysis.^[24]

To date, different fabrication techniques have been successfully utilized to realize $\text{Ag}_x\text{Au}_{1-x}$ alloyed NPs. They can be formed by colloidal synthesis via the reduction of precursors containing metals in solution,^[25,26] and by the sequential pulsed laser deposition of Ag and Au targets,^[27,28] which can yield large amounts of NPs with narrow size distribution. However, the overall size of the NPs cannot be varied beyond 150 nm.^[29] Alternatively, nanolithographic methods enable full control of NPs size, shape, and distribution.^[13] Nevertheless, this technique is constrained to specific applications due to its high cost and very limited scalability. The dewetting of metallic thin films has also been used to fabricate pure^[21,30–32] and alloyed^[19] metal NPs. In this simple and effective fabrication route, a very thin layer of metal (<50 nm) is initially deposited onto a substrate. Then, when the thin-film sample is annealed under a controlled environment (oxygen free), surface diffusion takes place and results in the formation of nanostructures to minimize the energy of the system.^[33–36] This method has been particularly useful for optoelectronic devices, where these metallic NPs act as light scattering centers that ultimately increase light absorption within the semiconductor.^[4,37]

In this work, we fabricate fully alloyed $\text{Ag}_x\text{Au}_{1-x}$ NPs with controlled chemical composition by dewetting thin films and characterize their optical response at the macro- and nano-scale. Surprisingly, we find that the NPs' distribution heavily depends on the thin-film chemical composition, irrespective of the original film thickness. Simultaneously, we measure a shift of the LSPR due to the NPs' composition variation, which defines their optical response. We map the elemental distribution of Ag and Au and confirm that the NPs are fully alloyed, forming a solid solution at the nanoscale. To further illustrate how the chemical composition affects the material optical response, we perform a detailed analysis of the optical characteristics of fully alloyed $\text{Ag}_{0.5}\text{Au}_{0.5}$ nanostructures in the visible range of the spectrum. For that, we combine spectrally dependent NSOM measurements and finite-difference time-domain (FDTD) simulations to locally resolve the optical response of individual NPs. Our results of the near-field light-matter interactions for $\text{Ag}_{0.5}\text{Au}_{0.5}$ nanostructures reveal an electric field enhancement of 30 times in the visible range of the spectrum under the NPs

C. Gong, G. C. Wessler, Dr. J. A. Taillon,
Prof. L. G. Salamanca-Riba, Prof. M. S. Leite
Department of Materials Science and Engineering
University of Maryland
College Park, MD 20742, USA
E-mail: mleite@umd.edu

C. Gong, Dr. M. R. S. Dias,
G. C. Wessler, Prof. M. S. Leite
Institute for Research in Electronics and Applied Physics
University of Maryland
College Park, MD 20742, USA



DOI: 10.1002/adom.201600568

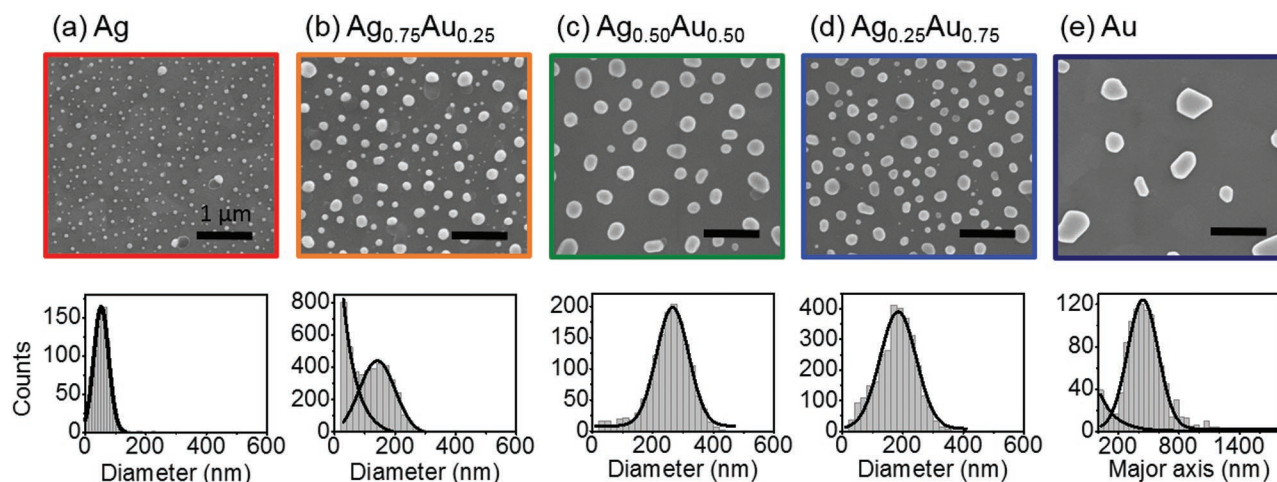


Figure 1. SEM plan-view images of a) Ag, b) $\text{Ag}_{0.75}\text{Au}_{0.25}$, c) $\text{Ag}_{0.5}\text{Au}_{0.5}$, d) $\text{Ag}_{0.25}\text{Au}_{0.75}$, and e) Au nanoparticles (NPs) showing size and shape distribution. The corresponding diameter statistics are shown on the second row, where the average diameter for each sample is 53 ± 29 , 141 ± 70 , 253 ± 62 , 184 ± 70 , and 441 ± 176 nm, respectively. Here, the uncertainties refer to the full-width-half-maximum of the Gaussian fits. For Au NPs the major axis of a hemispheroid is used to describe their size distribution.

and in its vicinity. The NSOM measurements are in excellent agreement with our full-field simulations.

We fabricate alloyed NPs by the cosputtering deposition of Ag and Au on indium tin oxide (ITO)/glass substrates, followed by a thermal annealing treatment under a controlled environment, as described in the Experimental Section. Upon annealing, the thin film suffers substantial surface diffusion, and the NPs are formed to minimize the nanoparticles + substrate system's energy (the surface and edge energy terms of the enthalpy).^[34] A sequence of scanning electron microscopy (SEM) plan-view images of the NP samples are presented in **Figure 1a–e**, with its corresponding diameter statistics. NPs are obtained across the whole composition range, from pure Ag to pure Au, using the same annealing condition (see Experimental Section for fabrication details). Hemispherical NPs are formed in all alloyed samples containing Ag, with average base diameter equal to 53 ± 29 , 141 ± 70 , 253 ± 62 , and 184 ± 70 nm for Ag, $\text{Ag}_{0.75}\text{Au}_{0.25}$, $\text{Ag}_{0.5}\text{Au}_{0.5}$, and $\text{Ag}_{0.25}\text{Au}_{0.75}$, respectively (see Table S1 and Figure S1 in the Supporting Information for statistics). The spatial distribution (density) of the particles corresponds to a coverage area of 7%, 12%, 19%, and 19%, respectively. The samples with $\text{Ag}_{0.75}\text{Au}_{0.25}$ and $\text{Ag}_{0.25}\text{Au}_{0.75}$ present NPs with similar average size, but different distribution (see **Figure 1**). In particular, we observe a large population of extremely small NPs on sample $\text{Ag}_{0.75}\text{Au}_{0.25}$, most likely resulting from incomplete ripening process, a common phenomenon defined by the coarsening of larger particles at the expense of smaller ones, resulting from their chemical potential minimization.^[38] Conversely, the pure Au NPs are faceted, with an average major and minor axis equal to 441 ± 176 and 368 ± 148 nm, where the substrate area covered by the NPs is 9%.^[39] The relatively strong cohesion between Ag and ITO leads to the formation of small particles, whereas the weak cohesion between Au and ITO gives rise to larger, faceted particles.^[33] Therefore, the combination of such properties resulted in a narrower size distribution for $\text{Ag}_{0.5}\text{Au}_{0.5}$ NPs, compared to the other samples.

To assess the potential of our scalable fabrication method to produce arrays of NPs with tunable LSPR, we analyze the optical response of the NPs at the macro- and nanoscale. **Figure 2** presents the measured and simulated transmission spectra for the $\text{Ag}_x\text{Au}_{1-x}$ system. For all samples containing Ag we observe well-defined resonance peaks, and a redshift of the LSPR by increasing the Au content. **Figure 2b** displays the photographs of the alloyed NPs on ITO/glass, where the corresponding colors of the samples are in agreement with the measured transmission spectra (due to their respective plasmon resonance). In order to corroborate our measurements, we use the FDTD method (see the Experimental Section for simulation details); our calculated transmission spectra are in good agreement with our measurements, as shown in **Figure 2c**. We calculate the transmission for NPs with average diameter and density obtained from **Figure 1**, mimicking the fabricated nanostructures. Because the dielectric function of metal alloys cannot be estimated as the linear combination of their pure counterparts,^[12] we use the experimentally determined index of refraction of the alloyed thin films (before annealing treatment) as the input in our calculations by combining transmission and reflection ellipsometry measurements (see **Figures S2–S4** in the Supporting Information). The small discrepancy observed on the width of the LSPR peak results from the fact that our calculations do not take into account the size and the random spatial distributions of the NPs, which is well known to affect the broadening of the LSPR.^[40–42] The chemical composition contributes to the redshift of the transmission (see **Figures S5 and S6** in the Supporting Information for NP size and morphology effects). Also, we observe a similar redshift on the LSPR from pure Ag to pure Au through the scattering and absorption efficiencies of perfectly spherical NPs using the Mie scattering theory (see **Figure S7** in the Supporting Information for details). The absence of a transmission peak for the pure Au sample is due to the very low density of NPs; because the peak shift of pure Au NPs has been extensively studied^[39] it is not the focus of this work.

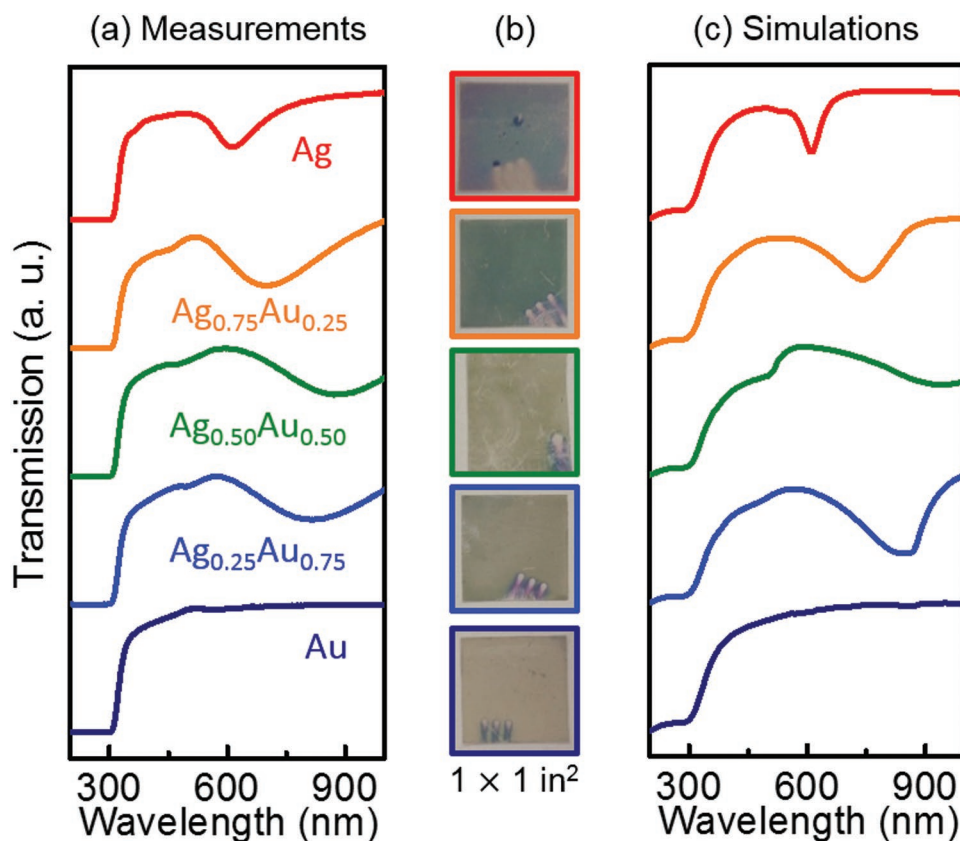


Figure 2. Macroscopic optical response of Ag–Au alloyed NPs. a) Measured transmission spectra of the $\text{Ag}_x\text{Au}_{1-x}$ NPs. b) Photographs of alloyed NPs on ITO/glass substrate on a white background. c) Finite-difference time-domain simulated transmission spectra.

To further evaluate if the fabrication method implemented here provides fully alloyed nanostructures, we perform energy-dispersive X-ray spectroscopy (EDS) elemental mapping on the $\text{Ag}_{0.5}\text{Au}_{0.5}$ sample, as shown in **Figure 3a**. We first mill the front and back of a representative NP using a Ga^+ focused ion beam (FIB) to minimize background signal from other NPs, see **Figure 3b**. Secondly, as presented in **Figure 3c–h**, we sequentially mill and image the NP to determine the elemental distribution within the structure and to confirm that no material segregation took place during the annealing treatment. A volumetric homogeneous distribution of both Ag and Au is detected within the NP, verifying that a solid solution is formed at the nanoscale, in agreement with the phase diagram for $\text{Ag}_x\text{Au}_{1-x}$ system.^[43] The amount of Ag and Au per NP is further confirmed by the plan-view EDS analysis of different NPs, which show an average chemical composition of $\text{Ag}_{0.54}\text{Au}_{0.46}$, (see **Figures S8 and S9 and Table S2** in the Supporting Information).

We probe the near-field optical response of the fully alloyed $\text{Ag}_{0.5}\text{Au}_{0.5}$ NPs sample by spectrally dependent NSOM measurements in illumination mode. Here, an Al-coated Si cantilever with a hollow SiO_2 pyramid tip with ≈ 60 nm aperture is scanned across the sample surface and the transmission signal is detected at the far-field with a $60\times$ objective lens located 0.3 mm underneath the sample. The topography and transmission signals are acquired simultaneously. As shown in **Figure 4a–e**, the NPs are well resolved throughout all measurements, indicating no significant tip changes during the scans. **Figure 4f–j** displays

the spectral dependence of the transmittance for the NPs within the visible range of the spectrum, from 500 to 700 nm. We observe high transmittance features irrespective of the illumination wavelength, both underneath and around the edges of the NPs (see **Figure S10** in the Supporting Information for more details). Nevertheless, there is a remarkable higher local transmission at 600 nm, compared to the scans acquired at other wavelengths. This singular characteristic results from the electric field enhancement caused by the particles' LSPR at 600 nm. In fact, the shape of the macroscopic transmission (see **Figure 2**) follows the same behavior revealed by the wavelength dependent NSOM scans, caused by the LSPR. As expected, the bare ITO shows high transmittance between 500 and 700 nm. **Figure 4k–o** shows simulated maps of the square modulus of the electric field ($|\mathbf{E}|^2$) underneath a hemispherical $\text{Ag}_{0.5}\text{Au}_{0.5}$ NP on ITO/glass substrate, using an unpolarized point dipole at the top of the NP as the illumination source,^[44] where the dashed lines refer to the NP size (see the Experimental Section for details). Our simulations are in excellent agreement with the NSOM measurements: at 600 nm the $|\mathbf{E}|^2$ is extremely high just below the NPs, at its center and around its edges. The $|\mathbf{E}|^2$ is very low on the ITO layer due to the fact that the simulations are performed using a dipole light source, instead of multiple ones throughout the simulation space.

To acquire the full picture of the near-field light-NPs interactions taking place, we simulate the cross-section electric field $|\mathbf{E}|^2$ decay as a function of wavelength. **Figure 5** shows $|\mathbf{E}|^2$

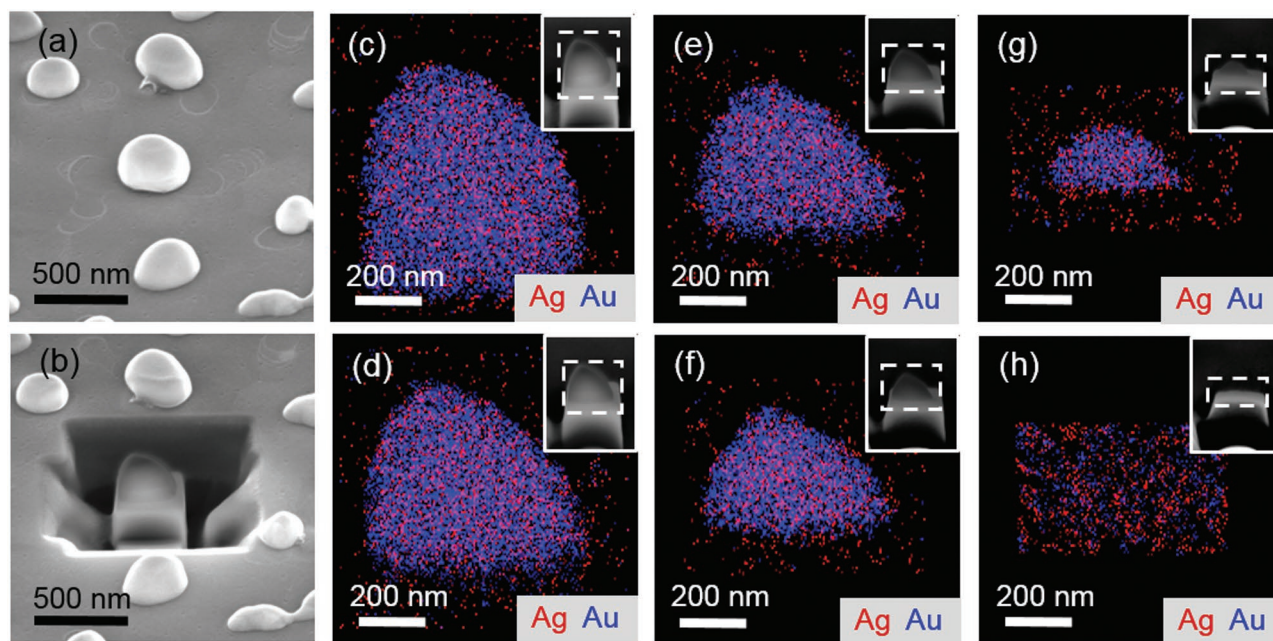


Figure 3. Fully alloyed Ag–Au nanoparticles. SEM images of a representative $\text{Ag}_{0.5}\text{Au}_{0.5}$ NP a) before and b) during FIB milling. c–h) EDS composition maps obtained during serial milling (70 nm slice thickness) of the NP, showing homogeneous distribution of Ag and Au throughout their volume, confirming the formation of a solid solution at the nanoscale. Insets: Cross-sectional SEM images of the NP after each milling step.

across a 253 nm hemispherical $\text{Ag}_{0.5}\text{Au}_{0.5}$ NP on top of a 70 nm ITO and 500 nm glass substrate. Due to the LSPR, the intensity of the electric field at 600 nm is enhanced 30 times around the

NP, in the ITO layer. Conversely, at 500 and 700 nm this effect is almost fully suppressed, and the field intensity in the substrate gradually diminishes. The overall decrease of the electric

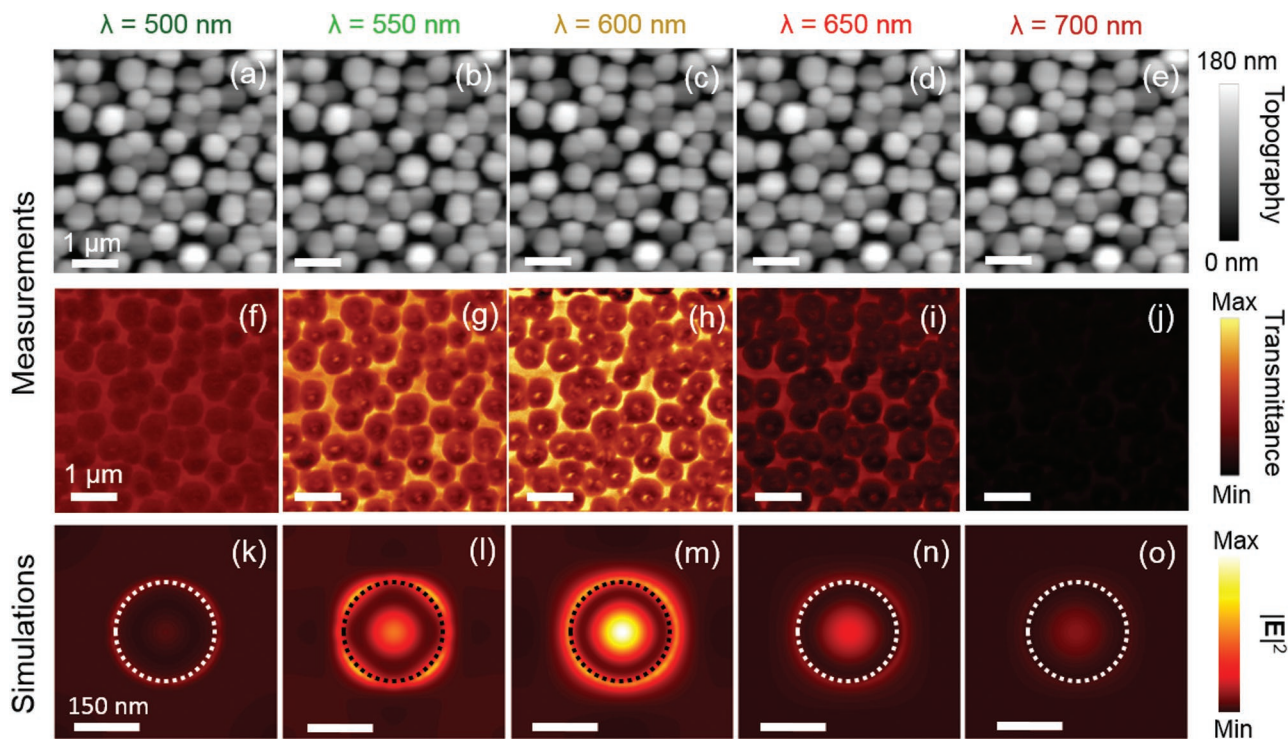


Figure 4. Near-field optical response of $\text{Ag}_{0.5}\text{Au}_{0.5}$ fully alloyed nanoparticles. a–e) Topography and f–j) NSOM transmittance measurements for representative $\text{Ag}_{0.5}\text{Au}_{0.5}$ NPs showing strong spectral dependence. k–o) FDTD simulation of the square modulus of the electric field ($|E|^2$) profile as a function of wavelength, where the dashed circles refer to the NP position. Illumination conditions: unpolarized point dipole located at the top of the NP.

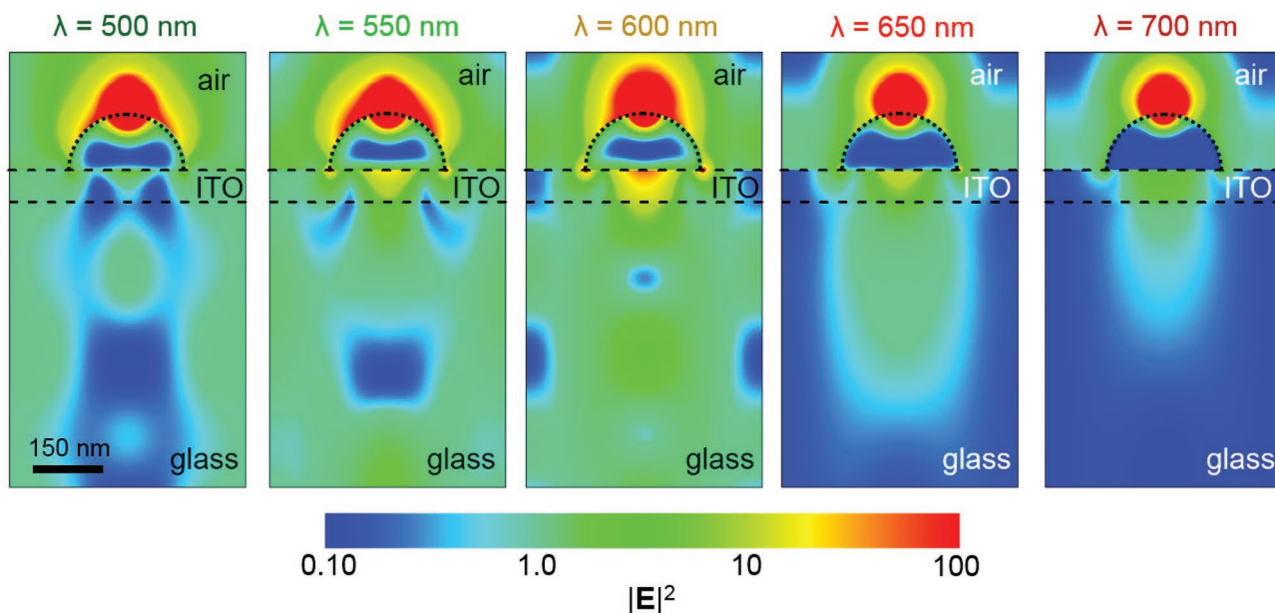


Figure 5. Full-field simulation of light-nanoparticle interaction at the nanoscale. Cross-section profile of the square modulus of the electric field $|E|^2$ for a 253 nm hemispherical $\text{Ag}_{0.5}\text{Au}_{0.5}$ nanoparticle on a 70 nm ITO/500 nm glass substrate as a function of wavelength. Illumination conditions: unpolarized point dipole at the top of the nanoparticle ($\lambda=500, 550, 600, 650,$ and 700 nm).

field intensity at 500 nm is not as strong as at 700 nm due to the proximity with the quadrupole LSPR, as shown by the transmission spectra in Figure 2. Moreover, at 700 nm a large fraction of the incident light is reflected by the NP, the electric field is screened, resulting in low transmittance. The calculated field profile agrees very well with the NSOM measurements, Figure 4f–j, which also shows a maximum transmittance at 600 nm, assisted by the LSPR.

In summary, we have investigated the optical properties of fully alloyed $\text{Ag}_x\text{Au}_{1-x}$ NPs at the macro- and nano-scale. Making use of a scalable and low-cost process, random and fully alloyed NPs were produced by the dewetting of alloyed thin films, with chemical composition ranging from pure Ag to pure Au. We found that the NPs' spatial distribution heavily depends on the original chemical composition of the thin film, instead of its thickness. As confirmed by EDS measurements, a uniform elemental distribution of Ag and Au was obtained for the $\text{Ag}_{0.5}\text{Au}_{0.5}$ sample demonstrating that a solid solution is formed at the nanoscale. We revealed the near-field effect of the LSPR in the alloyed NPs through spectrally dependent NSOM measurements. High local transmittance was observed both underneath and around the edges of the nanostructures. These measurements were in excellent agreement with our FDTD simulations, which showed that the $|E|^2$ in the vicinity of and within the particles strongly varies as a function of wavelength. Our results open the possibility to explore an additional knob to tune the LSPR in metallic nanostructures fabricated by a scalable physical approach: their chemical composition. By using different substrates, with distinct wettability, one could implement the method presented here to realize self-assembled alloyed nanostructures with a variety of chemical compositions and optical responses extended to a broader range of the spectrum. For instance, Al-based alloys could expand the functionality of some

optoelectronic devices that operate in the visible into the UV range of the spectrum.

Experimental Section

Fabrication of Alloyed NPs: Alloyed thin films were fabricated via the cosputtering deposition of pure Ag (99.99%) and Au (99.99%) at room temperature, with deposition rates calibrated to reach different nominal chemical compositions, ranging from Ag, $\text{Ag}_{0.75}\text{Au}_{0.25}$, $\text{Ag}_{0.5}\text{Au}_{0.5}$, $\text{Ag}_{0.25}\text{Au}_{0.75}$ to Au. During deposition, the sample stage was rotated at 8 rpm to ensure uniform elemental distribution within each thin-film sample. The thin films were deposited onto 1×1 in.² ITO (70 nm)/glass substrates that were previously cleaned with acetone and deionized water, then dried with N_2 . The as-obtained thin films were annealed at 600 °C for 1 h in N_2 flow of 1 atm to form the alloyed NPs.

Macroscopic Transmission Measurements: The transmission measurements were performed using an ellipsometer (200–1000 nm) at normal incidence, where the base line was air.

Chemical Composition Analysis: Surface and cross-sectional energy dispersive X-ray spectroscopy was performed using a dual-beam FIB/SEM, equipped with an EDS detector. Cross sections of the NPs were milled with a Ga^+ -ion beam current of ≈ 1 pA. Because the resolution of the EDS analysis is limited by the electron interaction volume (rather than by the beam size), probing thin sections of the NPs ensured a reliable analysis, with high spatial resolution. The relative composition of the particles was determined using the Au-M and Ag-L α X-ray lines (at characteristic energies of 2.120 and 2.984 keV, respectively), excited using a primary electron beam with a 10 kV accelerating voltage, ≈ 2 nA current, and a 100 μs dwell time.

Near-Field Transmission Measurements: A near-field scanning optical microscope coupled with a supercontinuum laser was used for the near-field transmission measurements. Unpolarized incident light was transmitted through the aperture (≥ 60 nm in diameter) of a NSOM probe and the signal was collected by a 60 \times objective lens with NA = 0.8, located 0.3 mm underneath the sample. Each transmission scan was conducted with the probe < 10 nm from the sample surface at the speed of 2 s/line, with 512 \times 512 points. The maps were then normalized by the incident photon flux, measured at each wavelength by a silicon photodetector positioned at the sample location.

Numerical Simulations: Numerical simulations were performed through the FDTD method. For the macroscopic transmission calculations, a normal incident plane wave source was used while an unpolarized point dipole source was used for the nanoscopic ones. A squared array of hemispherical Ag_{0.5}Au_{0.5} NPs on top of a semi-infinite substrate with a 70 nm ITO layer and glass was used in the simulation space to mimic the fabricated samples, replicating the size and density distributions of the sample. Perfect matched layer boundary conditions were used in the z-direction while periodic boundary conditions were used in the x- and y- in-plane directions. The broadband radiation of the plane wave light source was propagated from air into the substrate with the NPs on the front. For all simulations presented here, the index of refraction was modeled through the multi-coefficient material model using transmission and reflection ellipsometry measurements of the alloyed thin films before annealing as the input data (see Figures S2–S4 in the Supporting Information). Likewise, the same procedure was used in order to obtain the ITO index of refraction. For the glass substrate, SiO₂ Palik's data was used. The transmittance and electric field spatial distribution profile were calculated as a function of the wavelength for each simulation. Here, the net power flow out of a squared surface 500 nm below the substrate was used to calculate the transmittance within the simulation. Finally, the electric field spatial distribution was calculated from a cross-section rectangular surface, 515 nm wide and 570 nm deep in the substrate, centered with respect to the NP.

Supporting Information

Supporting Information is available from the Wiley Online Library or from the author.

Acknowledgements

C.G. and M.R.S.D. contributed equally to this work. The authors gratefully acknowledge E.M. Tennyson and A. Chang for fruitful discussions, the Maryland NanoCenter FabLab, NISPII Lab, and AIMLab for their technical support. The authors acknowledge financial support from the National Science Foundation, the Schlumberger Foundation Faculty for the Future, the 2014 Minta Martin Award, the 2015 Graduate School Summer Fellowship, and the ASPIRE Program at UMD. This material is based upon work supported by the National Science Foundation under Grant No. 1609414 (DMR), Grant No. HRD1008117 (ADVANCE/UMD program), and the Graduate Research Fellowship Program (Grant No. DGE 1322106). Research was performed in part at the NIST Center for Nanoscale Science and Technology.

Received: July 15, 2016
Revised: August 6, 2016
Published online:

- [1] Z. Feng, C. Jiang, Y. He, S. Chu, G. Chu, R. Peng, D. Li, *Adv. Opt. Mater.* **2014**, *2*, 1174.
- [2] S. A. Maier, *Plasmonics: Fundamentals and Applications*, Springer, New York **2007**.
- [3] M. A. Green, S. Pillai, *Nat. Photonics* **2012**, *6*, 130.
- [4] S. Pillai, K. Catchpole, T. Trupke, M. Green, *J. Appl. Phys.* **2007**, *101*, 093105.
- [5] S. Nie, S. R. Emory, *Science* **1997**, *275*, 1102.
- [6] K. P. García, K. Zarschler, L. Barbaro, J. A. Barreto, W. O'Malley, L. Spiccia, H. Stephan, B. Graham, *Small* **2014**, *10*, 2516.
- [7] C. T. Campbell, S. C. Parker, D. E. Starr, *Science* **2002**, *298*, 811.
- [8] S. A. Maier, M. L. Brongersma, P. G. Kik, S. Meltzer, A. A. Requicha, H. A. Atwater, *Adv. Mater.* **2001**, *13*, 1501.
- [9] W. Rechberger, A. Hohenau, A. Leitner, J. Krenn, B. Lamprecht, F. Aussenegg, *Opt. Commun.* **2003**, *220*, 137.
- [10] S. Graells, R. Alcubilla, G. Badenes, R. Quidant, *Appl. Phys. Lett.* **2007**, *91*, 121112.
- [11] K. Thyagarajan, C. Santschi, P. Langlet, O. J. F. Martin, *Adv. Opt. Mater.* **2016**, *4*, 871.
- [12] C. Gong, M. S. Leite, *ACS Photonics* **2016**, *3*, 507.
- [13] F. A. A. Nugroho, B. Iandolo, J. B. Wagner, C. Langhammer, *ACS Nano* **2016**, *10*, 2871.
- [14] A. Genc, J. Patarroyo, J. Sancho-Parramon, R. Arenal, M. Duchamp, E. E. Gonzalez, L. Henrard, N. G. Bastus, R. E. Dunin-Borkowski, V. F. Puentes, J. Arbiol, *ACS Photonics* **2016**, *3*, 770.
- [15] Y. Hashimoto, G. Seniutinas, A. Balčytis, S. Juodkazis, Y. Nishijima, *Sci. Rep.* **2016**, *6*, 25010.
- [16] Y. Liu, X. Zhang, *Chem. Soc. Rev.* **2011**, *40*, 2494.
- [17] C. Zhao, J. Zhang, Y. Liu, *EPJ Appl. Metamater.* **2014**, *1*, 6.
- [18] M. L. Brongersma, N. J. Halas, P. Nordlander, *Nat. Nanotechnol.* **2015**, *10*, 25.
- [19] M. Xu, J. Feng, Y.-S. Liu, Y. Jin, H.-Y. Wang, H.-B. Sun, *Appl. Phys. Lett.* **2014**, *105*, 153303.
- [20] S. Liu, R. Jiang, P. You, X. Zhu, J. Wang, F. Yan, *Energy Environ. Sci.* **2016**, *9*, 898.
- [21] R. Yu, P. Mazumder, N. F. Borrelli, A. Carrilero, D. S. Ghosh, R. A. Maniyara, D. Baker, F. J. García de Abajo, V. Pruneri, *ACS Photonics* **2016**, *3*, 1194.
- [22] C. W. Hsu, B. Zhen, W. Qiu, O. Shapira, B. G. DeLacy, J. D. Joannopoulos, M. Soljacic, *Nat. Commun.* **2014**, *5*, 3152.
- [23] J. Olson, A. Manjavacas, L. Liu, W.-S. Chang, B. Foerster, N. S. King, M. W. Knight, P. Nordlander, N. J. Halas, S. Link, *Proc. Natl. Acad. Sci. USA* **2014**, *111*, 14348.
- [24] J.-H. Liu, A.-Q. Wang, Y.-S. Chi, H.-P. Lin, C.-Y. Mou, *J. Phys. Chem. B* **2005**, *109*, 40.
- [25] G. Guisbiers, R. Mendoza-Cruz, L. Bazán-Díaz, J. J. Velázquez-Salazar, R. Mendoza-Perez, J. A. Robledo-Torres, J.-L. Rodríguez-Lopez, J. M. Montejano-Carrizales, R. L. Whetten, M. José-Yacamán, *ACS Nano* **2016**, *10*, 188.
- [26] S. Link, Z. L. Wang, M. A. El-Sayed, *J. Phys. Chem. B* **1999**, *103*, 3529.
- [27] S. Verma, B. T. Rao, A. P. Detty, V. Ganesan, D. M. Phase, S. K. Rai, A. Bose, S. C. Joshi, L. M. Kukreja, *J. Appl. Phys.* **2015**, *117*, 133105.
- [28] D. Rioux, S. Vallières, S. Besner, P. Muñoz, E. Mazur, M. Meunier, *Adv. Opt. Mater.* **2014**, *2*, 176.
- [29] D. Rioux, M. Meunier, *J. Phys. Chem. C* **2015**, *119*, 13160.
- [30] E. Thouti, N. Chander, V. Dutta, V. K. Komarala, *J. Opt.* **2013**, *15*, 035005.
- [31] M. Schmid, J. Grandidier, H. A. Atwater, *J. Opt.* **2013**, *15*, 125001.
- [32] J. Okumu, C. Dahmen, A. Sprafke, M. Luysberg, G. Von Plessen, M. Wuttig, *J. Appl. Phys.* **2005**, *97*, 094305.
- [33] C. V. Thompson, *Annu. Rev. Mater. Res.* **2012**, *42*, 399.
- [34] T. Zhai, Y. Wang, H. Liu, X. Zhang, *Opt. Express* **2015**, *23*, 1863.
- [35] C. T. Campbell, *Surf. Sci. Rep.* **1997**, *27*, 1.
- [36] S. Sabine, G. P. Vera, M. Mael, B. Rabah, *Nanotechnology* **2008**, *19*, 195712.
- [37] H. R. Stuart, D. G. Hall, *Appl. Phys. Lett.* **1998**, *73*, 3815.
- [38] M. S. Leite, T. I. Kamins, R. S. Williams, G. Medeiros-Ribeiro, *J. Phys. Chem. C* **2012**, *116*, 901.
- [39] A. Kossov, V. Merk, D. Simakov, K. Leosson, S. Kéna-Cohen, S. A. Maier, *Adv. Opt. Mater.* **2015**, *3*, 71.
- [40] F. Beck, A. Polman, K. Catchpole, *J. Appl. Phys.* **2009**, *105*, 114310.
- [41] Y. Nishijima, J. B. Khurgin, L. Rosa, H. Fujiwara, S. Juodkazis, *ACS Photonics* **2014**, *1*, 1006.
- [42] Y. Nishijima, J. B. Khurgin, L. Rosa, H. Fujiwara, S. Juodkazis, *Opt. Express* **2013**, *21*, 13502.
- [43] H. Baker, H. Okamoto, *ASM Handbook, Volume 03 - Alloy Phase Diagrams*, ASM International, Materials Park, OH, USA **1992**.
- [44] L. Novotny, B. Hecht, *Principles of Nano-Optics*, Cambridge University Press, New York, NY, USA **2006**.